JACERS-48254
Revised manuscript

Originally submitted to *J. Am. Ceram. Soc.*
August 26, 2021

Microstructural and infiltration properties of woven preforms during chemical vapor infiltration

Chong M. Cha*[,1] David Liliedahl[2] Ramanan Sankaran[3] Vimal Ramanuj[3]

[1] *Composites Technology Center*
Rolls-Royce Corporation
546 S. Meridian St.
Indianapolis, IN 46225

[2] *Combustion & Turbines*
Rolls-Royce Corporation
546 S. Meridian St.
Indianapolis, IN 46225

[3] *Computational Sciences and Engineering*
Oak Ridge National Laboratory
Oak Ridge, TN 37831

Abstract

Interface resolved direct numerical simulations (DNS) of chemical vapor infiltration (CVI) have been performed over a range of furnace operating conditions (Thiele moduli) and for practical woven preform geometries. A level-set method is used to resolve the geometry of the initial preform at tow scale. The interface between the vapor and solid phase is then evolved in time through the entire CVI densification cycle, fully resolving the time varying topology between the two phases [1]. In contrast to previous level-set methods for CVI simulation [2, 3], the physical reaction and diffusion processes govern the level-set movement in the current approach. The surface deposition kinetics is described by the usual one-step model. In this paper, the DNS data is used to study the evolving porosity, surface-to-volume ratio, and flow infiltration properties (permeability and effective diffusivities). Comparisons are made to popularly-assumed structure functions and the standard, Kozeny-Carmen porous media model commonly employed in modeled CFD simulations of CVI [4, 5]. The virtual DNS experiments reveal a Thiele modulus and preform geometry (fabric layup) dependence which the existing microstructural and infiltration models are not able to describe throughout the entire densification process. The DNS-based, woven geometry-specific correlations can be applied directly to mean-field, furnace-scale CFD simulations.

Notice: This manuscript has been authored by UT-Battelle, LLC, under contract DE-AC05-00OR22725 with the US Department of Energy (DOE). The US government retains and the publisher, by accepting the article for publication, acknowledges that the US government retains a nonexclusive, paid-up, irrevocable, worldwide license to publish or reproduce the published form of this manuscript, or allow others to do so, for US government purposes. DOE will provide public access to these results of federally sponsored research in accordance with the DOE Public Access Plan (http://energy.gov/downloads/doe-public-access-plan).

*Corresponding author. E-mail: `chong.cha2@rolls-royce.com`, Tel: (317)820-7197

1 Introduction

Materials processing by chemical vapor deposition/infiltration (CVD/CVI) is fundamental in advancing materials fabrication for semiconductor, microelectronic, optics, nuclear, friction (brakes), and propulsion applications [6]. For example, in the gas turbine industry, silicon-carbide (SiC) reinforced ceramic matrix composites (CMCs) offer higher temperature capability over metallic superalloys at significantly reduced weight. CMCs are thus currently a key enabling technology to realize the reduced fuel consumption and greener emissions necessary to sustain the continual, rapid growth in the air transportation industry.

A primary challenge in adopting CMC materials is reducing their high cost of manufacture, due in part to the long CVI densification times. The long CVI processing times are needed to ensure uniform chemical deposition of the matrix, which can only occur if the vapor species involved in the deposition processes can completely infiltrate and egress from the complex evolving network of flow channels. The fluid network is initially characterized by the preformed geometry of the engineered component. Fibers (each typically of order 10 μm in diameter) are collected into yarns or tows ($\sim$1 mm in diameter) and woven into fabric-like plys, *e.g.*, the industry standard, five-harness satin (5HS) weave. The woven plys are used to construct the preform geometry of the engineering component ($\sim$10 cm or larger). The initial preform is mostly void of the solid (fiber) material. The desired material properties of the final processed components are governed by the initial preform geometry and the final porosity, uniformity, and chemical makeup of the densified part.

A simple (one-step, irreversible) representative model of the chemical reaction is

$$\mathcal{A} \xrightarrow{k} \mathcal{B}(s) + \mathcal{C} \ . \tag{1}$$

This equation represents a precursor vapor $\mathcal{A}$ depositing a solid phase $\mathcal{B}(s)$, while emitting by-product $\mathcal{C}$. For example, in the SiC matrix CMC application, $\mathcal{B}(s)$ is SiC, species $\mathcal{A}$ its reagent (*e.g.*, methyltrichlorosilane) and $\mathcal{C}$ the by-product (*e.g.*, HCl). The rate of this first-order reaction (k) is a strong function of temperature.

The optimisation of the CVI manufacturing process and motivation of this work is illustrated in Fig. 1, which shows a region near the part boundary. The dark blue circles are the preform geometry (cross-section of the fibers), the deposited solid matrix material ($\mathcal{B}$) is in grey, and the surrounding colors measure the concentration of vapor species ($\mathcal{A}$). Highest concentrations are red, lowest in blue. Here, $\mathcal{A}$ diffuses into the preform from above. Figure 1 (a) illustrates an unoptimized process where, for example, the uniform furnace temperature is too low making reaction Eq. (1) slow with respect to the transport of $\mathcal{A}$. The result is good, uniform growth in the matrix throughout the part, but at the costly expense of a long manufacturing time.

In (b), the furnace temperature has been increased, thereby increasing the chemical deposition rate. As a result, at the same processing time as in (a), the relatively fast matrix growth on the surface of part (b) creates a large, vacuous region that can no longer be infiltrated by the reagent $\mathcal{A}$.

Optimizing the CVI manufacturing process at practical, production scales is made further challenging by the necessarily large CVI furnaces. On production furnace scales ($\sim$1 m), maintaining isothermal and isobaric conditions is challenging, which results in part-to-part densification differences due to the temperature and gas non-uniformities. Addressing these macroscopic non-uniformities further adds to the time and cost of CVI manufacturing. Although the Reynolds numbers are low, the range of lengthscales required to computationally resolve the furnace flow spans six orders-of-magnitude. The chemical reactions further increase the computational demand. While the present work represents the first time Direct Numerical Simulation (DNS) has been applied to CVI, current supercomputing capability is still unable to resolve the full range of scales of practical interest. That is, to optimize the furnace loading of a given set of parts, the furnace-scale CFD simulations must employ mean-field transport or porous media models at unresolved part scales. This further requires microstructural evolution properties to be assumed or modeled.

The standard model characterizing the momentum loss and the effective mass and energy fluxes through any porous media is

$$\begin{aligned} B &= \frac{1}{C_1}\frac{\phi^3}{\sigma^2} && \text{(2a)} \\ \mathcal{D}_{\mathrm{eff},j} &= \frac{\phi}{C_2}\mathcal{D}_{j,\mathrm{mix}} && \text{(2b)} \\ \lambda_{\mathrm{eff}} &= \phi\lambda + (1-\phi)\lambda_s \ . && \text{(2c)} \end{aligned}$$

Here, B is the permeability, ϕ is the volume porosity, σ is the surface-to-volume ratio, C_1 is the Kozeny-Carman constant, $\mathcal{D}_{\mathrm{eff},j}$ is the effective diffusivity of the j-th species, $\mathcal{D}_{j,\mathrm{mix}}$ is the molecular (free) diffusivity, C_2 is the tortuosity parameter, and λ_{eff} is the effective conductivity with λ and λ_s the thermal conductivities of the gas and solid, respectively. It is currently unknown whether the calibration of the constants C_1 and C_2 needed in "post-dicting" densified CVI parts is due to limitations of the infiltration model Eq. (2) or other modeling assumptions like the assumed chemical kinetics or the modeled microstructural properties.

Numerous models exist to approximate the microstructural properties of woven preforms needed for Eq. (2) [7, 8, 9, 10]. (Specific examples are described later in the paper.) The goal of these models is to relate the porosity, surface-to-volume ratio, and one or more lengthscales throughout the preform densification. A quasi-steady approximation is invoked by assuming analytical expressions or structure functions for the interdependence of the microstructural properties, *e.g.*, $\sigma = f(\phi, D)$, where D is some effective lengthscale of the porous media. Improvements to the models have been made by introducing additional lengthscales like the tortuosity [11]. However, the tortuosity has been shown to be a function of the flow and not geometry alone [12], making it difficult to specify the tortuosity with only a given preform geometry. While impressive advancements have been made to measure the microstructural properties using high-resolution X-ray tomography [13, 14], characterization of the states throughout the entire CVI densification cycle has not been achieved.

In this paper, we report on recent direct numerical simulations (DNS) of CVI over the complete densification cycle, from dry fabric to the final time, when the ultimate porosity is reached [1]. The DNS approach fully resolves the continuum scales, thus a porous media model is not required. Further, the geometry evolves due to the fundamental physical processes, and so the microstructural states do not need to be assumed or modeled. A level-set method tracks the complex topology between the vapor and solid phases. The one-step deposition model Eq. (1) employed in the DNS, and commonly assumed in CVI furnace-scale CFD simulations, is an incomplete description of the kinetic processes [15, 16, 17, 18, 19, 20, 21]. A comprehensive DNS would also require the use of a detailed chemical kinetic model to describe the pyrolysis of the CVI reagents and surface deposition reactions. However, employing a detailed kinetic model would have prohibitively increased the cost of the simulations. The one-step kinetic model allowed us to perform the requisite high resolution simulations and sensitivity studies with the DNS. Future extensions to include complex (multi-step) chemical kinetics are needed to realize the full potential of DNS. Similarly, only the diffusive transport of the precursors by Fickian diffusion has been invoked, again leaving more advanced extensions (*e.g.*, Knudsen diffusion effects) for future work. Despite these approximations, the resulting "simplest-no-simpler" DNS can be used to study the key fundamental physical interactions between the transport, chemistry, and evolution of the porous media geometry. The datasets produced by the DNS also allow the evaluation of porous media models for engineering scale CFD simulations. Due to the high spatial resolution requirements of DNS, the simulated domain size is usually restricted to small domains, a single unit cell of the preform in the present case. The size of the unit cell and the DNS domain is on the order of ∼1 cm^3 (the size of a typical, single computational cell of a CVI furnace-scale CFD simulation). Even at this scale, massively parallel computing resources are required for the DNS. The Titan supercomputer at the Oak Ridge National Laboratory was used for the DNS cases presented here.

The first application of level-set methods to CVI was made by Jin and co-workers on simplified, two-dimensional geometries [2, 22, 23]. Guan and co-workers [3, 24] applied a similar level-set method, advancing the capability to include practical 3-D woven geometries. In these previous approaches, a calibrated Stefan velocity is imposed on the moving interfaces or is prescribed a constant value everywhere, thus ignoring local interactions with the finite-rate chemical kinetic timescale. To further advance these previous approaches, physical reactive-diffusive processes are used to govern the level-set dynamics in the present work. This allows local deposition gradients to develop in the part (*e.g.*, as illustrated in Fig. 1) from the flow rather than from the geometry alone.

The paper is organized as follows. Section 2 gives a description of the CVI model. Section 3 presents the results from the virtual DNS experiments, which are performed under isobaric and isothermal processing conditions. The suite of testcases include varying the initial preform geometry and the Thiele modulus (related to the CVI model in Sec. 2). The initial preform geometries considered here include three different layup strategies of 5HS woven plys. The flow infiltration properties are quantified and their scaling behavior compared to the standard model, Eq. (2). The microstructural properties from the DNS are compared to the quasi-steady microstructural models of Sheldon & Besmann [8] and Ofori & Sotirchos [7]. These structure functions have been chosen with hindsight, having approximately bound the DNS data. Concluding remarks are given in Sec. 4.

2 Model

The level-set method is a general mathematical treatment to handle implicit geometries [25]. The method is particularly well-suited to describe the movement of complex topologies but generally requires specialized numerical treatments depending upon the particular physical application [26]. The level-set captures the interface implicitly without the need for time consuming body fitted mesh generation. The level-set function, φ, is defined as a continuous function such that it satisfies the distance property

$$|\nabla \varphi| = 1. \tag{3}$$

For the CVI application, the level-set $\varphi(\mathbf{x}, t) = \varphi_0$ represents the interface between the vapor and solid phases, which is the deposition front. Values greater than or less than φ_0 represent the vapor and solid phases respectively. Motion of the front is modelled by transporting the level-set in time. In the formulation here, care is taken to assign a physical basis for the movement of the level-set. Although novel advancements have also been made in the numerical treatment as part of this work [27], this section only summarizes the governing equations used in the DNS. A complete description of the model, including the detailed numerical solution procedure, can be found in [1, 27].

2.1 Physical Model

The general level-set equation is

$$\begin{aligned} \frac{\partial\varphi}{\partial t} + \mathbf{u}_s \cdot \nabla\varphi &= 0 && (4a) \\ \text{with} \quad \mathbf{u}_s &\equiv u_s \frac{\nabla\varphi}{|\nabla\varphi|} \ , && (4b) \end{aligned}$$

where $\mathbf{u}_s$ is the level-set velocity. For the CVI application, the chemical vapor deposition of $\mathcal{B}(s)$ in Eq. (1) defines the physical velocity for the φ_0 level-set. The magnitude of this velocity is the growth rate of the deposit, which Eq. (1) gives as

$$u_s = \frac{\dot{\omega}_s}{\rho_s} = \frac{A}{\rho_s} \exp\left(-\frac{T_a}{T}\right) Y \ . \tag{5}$$

Here, $\dot{\omega}_s$ (kg/m^2/s) is the surface chemistry deposition rate, ρ_s is the constant density of $\mathcal{B}(s)$ the bulk phase, A is the pre-exponential factor, T is the temperature, T_a is the activation temperature, and Y is the mass fraction of vapor $\mathcal{A}$. The direction of growth is always normal to the φ_0 level-set and thus, $\mathbf{u}_s$ is normal to the local level-set, $\varphi(\mathbf{x}, t)$. Note that the growth rate in the above expression can also be extended to include multi-step deposition kinetics.

The mass fraction is normalized as $C \equiv Y/Y_{\text{ref}}$, where Y_{ref} is its far-field value away from the preform. C is then unity at the far-field and zero when all of the reactant has been consumed. A mass balance for the scalar mass fraction of the gaseous reactant on the deposition front is

$$\frac{\mathcal{D}}{l_{\text{ref}}} \left.\frac{\partial C}{\partial n}\right|_{\varphi=\varphi_0} = \frac{\dot{\omega}_s}{\rho} \ , \tag{6}$$

where $\mathcal{D}$ is the mass diffusivity of the gaseous reactant, n is the non-dimensional normal coordinate on the interface, ρ is the gas density, and l_{ref} is a reference length scale. The DNS experiments here assume isothermal and isobaric conditions, so $\mathcal{D}$ and ρ are constant.

The non-dimensional Thiele modulus can be derived as the ratio of the diffusive time scale to the chemical time scale as

$$K = \frac{A \exp\left(-T_{\text{A}}/T\right) l_{\text{ref}}}{\rho\mathcal{D}} \ . \tag{7}$$

Then Eq. (6) becomes

$$\left.\frac{\partial C}{\partial n}\right|_{\varphi=\varphi_0} = KC|_{\varphi=\varphi_0} \ . \tag{8}$$

With the constant $\mathcal{D}$ for the present DNS experiments, the governing equation for the diffusive transport of the scalar C in the domain is

$$\nabla^2 C = 0 \ , \tag{9}$$

subject to the boundary condition Eq. (8) on the interface and the farfield boundary condition $C = 1$.

The fluid and solid phase interface is defined as the $\varphi(\mathbf{x}, t) \equiv 0$ contour and its movement is captured by advancing the level-set function in time. The velocity with which the interface moves is determined by the chemical deposition rate and the density of the solid matrix. Define a reference velocity scale by taking the reference, far-field value of the mass fraction in Eq. (5), or

$$u_{\mathrm{ref}} = \frac{A}{\rho_s} \exp\left(-\frac{T_a}{T}\right) Y_{\mathrm{ref}} \ . \tag{10}$$

Then the non-dimensional velocity at the interface is $S \equiv u_s/u_{\mathrm{ref}} = C$ acting normal to the interface $\varphi_0 \equiv 0$. As is customary in the level-set methods, the interface velocity is then propagated throughout the domain such that it satisfies

$$\nabla S \cdot \nabla \varphi = 0 \ , \tag{11}$$

subject to the condition $S = C$ at $\varphi = 0$. The computed velocity S is used to advance the level-set function using

$$\frac{\partial \varphi}{\partial \tau} + S|\nabla \varphi| = 0 \ , \tag{12}$$

where τ is the non-dimensional time. Periodic reinitialization of the level set function is necessary to ensure its signed distance property is retained. Here, the reference time scale, t_{ref} is defined using l_{ref} and u_{ref} as

$$t_{\mathrm{ref}} \equiv \frac{l_{\mathrm{ref}}}{u_{\mathrm{ref}}} = \frac{l_{\mathrm{ref}} \rho_{\mathrm{s}}}{A \exp\left(-T_{\mathrm{A}}/T\right) Y_{\mathrm{ref}}} = \frac{l_{\mathrm{ref}}^2}{\mathcal{D}} \frac{\rho_{\mathrm{s}}}{\rho Y_{\mathrm{ref}} K} \ , \tag{13}$$

a function of the Thiele modulus K.

The Thiele modulus does not appear in the previous CVI applications of the level-set method. In the approach by Guan and co-workers [3, 24], the level-set velocity is taken as a global constant. In this case, the densification is only a function of the geometry. In reality, the in-part densification gradients and inaccessible pores develop due to the flow (Thiele modulus effects) and not geometry alone. These fundamental physical effects are described by the present DNS model. In the approach by Jin and co-workers [2, 22, 23], the level-set velocity is prescribed as

$$u_s \equiv p(t, \mathbf{x}) K_1 \left(1 + K_2 \frac{\partial c}{\partial \mathbf{n}} + K_3 F(\kappa) \right) \quad , \tag{14}$$

where K_1, K_2, and K_3 are calibration constants, κ is the local curvature of φ, and $p(t, \mathbf{x})$ is a binary "switch" used during the calculations to stop the local level-set movement when an inaccessible void has been detected. The calibration constants and $F(\kappa)$ are not known *a priori*, but must be calibrated for each individual preform geometry and CVI processing condition. In contrast, for u_s defined by (5), no calibration constants are required. Only the fundamental flow and chemical kinetic properties are needed, which do not depend on any preform geometry or CVI processing condition. An artificial $p(t, \mathbf{x})$ parameter to handle inaccessible voids is not needed in the DNS due to the diffusive-reactive transport of reactant.

2.2 Implementation

Equation 4b is discretized in space using a third order (High Order) Upstream Central (HOUC3) scheme and is integrated in time using a fourth order explicit Runge-Kutta method. As the speed is a function of the local concentration, advection of the level-set does not guarantee that Eq. 3 will be satisfied. Periodic reinitialization is necessary, which often creates artificial movement of the interface leading to unphysical mass loss/gain. Mass conservation has remained a challenge in the implementation of the level-set method. In the current work, a high order accurate anchoring and fast sweeping method has been applied to improve the mass conservation property [27]. The method solves Eq. 3 away from the interface with a second order upwind discretization. The grid points adjacent to the interface are initialized with a second order accurate algebraic anchor. Detailed formulation of the anchoring and fast sweeping method can be found in Ref. [27].

Transport equation for C is solved in the void spaces (vapor phase) by applying the non-linear boundary condition given in Eq. 8 on the deposition front and farfield Dirichlet conditions. Standard second order central discretization is used to solve Eq. 9. The discretization stencil at a point close to the interface may include neighboring grid points belonging to a different domain (ghost domain) where physical value of the concerned variable is not available. A ghost fluid based immersed boundary method outlined in Ref. [28] is used to populate the grid points across the front. The transport equation is solved using an under-relaxed

Jacobi iterative solver. Expansion of C in the ghost (solid) domain around the interface can be written as

$$C_{\text{ghost}} = C|^{0}_{\varphi=\varphi_0} + \left.\frac{\partial C}{\partial n}\right|_{\varphi=\varphi_0} \varphi_{\text{ghost}} \ , \tag{15}$$

where quantities on the interface are interpolated from the real (void) domain. Concentration value on the front from previous iteration $C|^{0}_{\varphi=\varphi_0}$, is used in Eq. (8) to compute the normal gradient on the deposition front $\partial C/\partial n|_{\varphi=\varphi_0}$, which is imposed as a Neumann condition for the solution of Eq. (9). Upon convergence, the transport equation is satisfied along with the non-linear boundary condition on the front. The front propagation speed at grid points adjacent to the interface (including ghost points) is calculated as a function of $C|_{\varphi=\varphi_0}$. The speed is then propagated to grid locations away from the interface using a fast sweeping method similar to the one used for the level-set reinitializaiton.

The formulation and model described here is implemented in the code Quilt, which is an interface resolved finite difference solver being developed at Oak Ridge National Laboratory. The code uses the level-set method to capture dynamic multi-material interfaces. All the physics capabilites in the code (incompressible flow, heat and mass transfer) use the level-set based embedded boundary formulation to account for interfacial physics (e.g. surface tension, phase transformation, heterogeneous kinetics, etc.) and to apply complex boundary conditions on the interface. The approach enables computationally efficient representation of resolved interfaces by avoiding expensive surface mesh based approaches. Explicit Euler as well as second order implicit time integration methods are available. Spatial discretization is second order in space for all transport equations. Level-set is solved using a third order upstream central scheme and is reinitialized using the second order anchoring and fast sweeping scheme. The code is written in C++ and uses MPI and Kokkos [29] to enable distributed memory parallelism and portability to modern computational facilities with GPU architectures. The code has been ported to various supercomputers including Summit at Oak Ridge Leadership Computing Facility (OLCF). The computational performance of Quilt for the present application is mainly determined by the performance and scalability of the level set solver (Eqs. 11 and 12). In an earlier work [27], we have presented details on the numerical treatment and implementation of the level set solver and its parallel performance. A weak scaling study of the level set algorithm was performed using a periodic array of spheres and the scalability of the method was demonstrated on 4000 nodes of the Titan supercomputing system. Furthermore, the performance studies showed that the computational time was reduced by a factor of 2.5 when utilizing the GPU accelerators on Titan.

The initial geometry of the multi-layered weave preform is modeled using the TexGen software. The unit cell pattern of the 5HS weave is created with tow scale resolution without resolving the individual fibers that constitute a tow. The weave geometry is then exported in the stereolithography (STL) file format for input to Quilt. Quilt reads a single layer of the 5HS weave and applies further geometric transformations to create multiple layers with specified or random offsets. The initial interface is represented implicitly on the structured mesh using the level set function, which allows the interface to be evolved in time on the same structured mesh without requiring remeshing. To resolve the unit cell of a 5HS woven preform required 840 cells in each dimension, or 592.7 million cells total.

3 Results and discussion

Simulations are performed for a specified non-dimensional Thiele modulus,

$$K \equiv \frac{\tau_{\text{diff}}}{\tau_{\text{chem}}} \ . \tag{16}$$

Equation (7) gives the Thiele modulus in terms of the constant physical parameters of the present DNS experiments. Here, the Thiele modulus can be interpreted as the CVI processing operating condition (the fixed pressure and isothermal temperature determining the diffusivity and chemical kinetic rate), or as the local one at the pressure and temperature of a single computational cell in a furnace scale CFD simulation.

Figure 2 shows partially-densified weaves from the simulations for two representative, constant Thiele moduli of (b) $K = 0.001$ and (c) $K = 0.1$. The ultimate porosity has been reached in both cases. In Fig. 2 (a), the initial unit-cell 5HS woven preform that was used in both CVI simulations is shown. Here, the reactants diffuse into the preform from both the top and bottom, the vertical or through-thickness direction.

For $K = 0.001$, $\tau_{\text{diff}} << \tau_{\text{chem}}$ and the ultimate porosity is low due to the relatively fast diffusive transport as compared to the chemistry. For $K = 0.1$, the chemistry is sufficiently fast as compared to diffusive transport and the ultimate porosity is relatively high due to the pore closures at the outer plys. Figures 3 and 4 show cross-sections for the $K = 0.001$ and and $K = 0.1$ cases, respectively, at the (a) initial and (b) near the final times. Subplots (b) qualitatively illustrates the pore closures for the $K = 0.001$ case (Fig. 3) and $K = 0.1$ case (Fig. 4).

The virtual DNS experiments can also be used to understand residual porosity (manufacturing quality) trends for different preform geometries, as well as trends in the densification times (manufacturing times) as a function of a preforming strategy. Continuing the precedence established by Guan and co-workers in their level-set studies [3, 24], impermeable tows are used for the geometric model of the 3-D woven fabric geometry. Here, three ply layup geometries are considered:

- The **Baseline** case, shown above in Fig. 2 (a), is defined by the random layup of the individual woven plys. This is the common method of preforming.
- In the **Aligned** configuration, all the plys are vertically aligned and therefore this preform geometry is characterized by the lowest geometric tortuosity.
- In the **Overlap** case, each ply is offest from its adjacent ply such that all even and odd numbered plys are vertically aligned. A fixed offset of half a tow is used to yield the maximum geometric tortuosity through this weave.

In all three configurations, the individual 5HS woven plys are identical, the total number of plys are the same, and the total preform volume is the same. That is, the bulk porosity, surface area, and surface-to-volume ratio are the same initially. Since each idealized ply consists of identical tow sizes and tow spacings, all three preform geometries above (Baseline, Aligned, and Overlap) are characterized by the same geometric lengthscale. The choice of this lengthscale varies with the particular microstructural property model assumed by the manufacturing engineer [7, 8, 9, 10], but generally depends only upon the preform geometry (examples are given below in Sec. 3.1) and not on the flow (CVI operating conditions or Thiele modulus).

In the remainder of this section, the microstructural and infiltration properties are presented for only the idealized preform geometries above (Baseline, Aligned, and Overlap), and for a Thiele modulus of $K = 0.001$, 0.1, and an intermediate value of $K = 0.01$.

3.1 Microstructural properties

The goal of microstructural modeling is to provide a geometric description of the unresolved deposition fronts over the entire CVI densification cycle for a given mesoscopic scale, *e.g.*, the computational cell size in a furnace-scale CFD simulation.

In furnace-scale CFD simulations, the local porosity is known from the concurrent solution of

$$\frac{d}{dt}\phi = -\sigma k Y \quad , \tag{17}$$

given here for the present simplified, one-step deposition chemistry case Eq. (1). The simplest closure is obtained with a model for the surface-to-volume ratio (σ), which introduces additional modeling requirements for at least one lengthscale.

A model which is well-suited for CFD application is given by Ofori & Sotirchos [7]. In their approach, a flow network of random overlapping capillary tubes is used to model σ in terms of any ϕ as

$$\sigma = \frac{4}{D_0}\sqrt{-\log(1-\phi_0)}(1-\phi)\sqrt{-\log(1-\phi)} \ , \tag{18a}$$

where ϕ_0 is the initial porosity and D_0 is the constant lengthscale of the open (flow) channels, characterized by the fiber diameter in practice. Since the actual woven fiber geometry is modeled by a surrogate flow network, Eq. (18a) does not satisfy the actual initial surface area of woven fiber preforms. Examples of modeled CFD applications of Eq. (18a) can be found in [4, 5]. For the woven fabric preform cases considered here, predictions from this popular CFD model of σ computed directly from the DNS can be made using the normalized quantity σ/σ_0, where σ_0 is the initial surface-to-volume ratio of the preform. In the CFD model, σ_0 is given by Eq. (18a) with $\phi = \phi_0$, which upon normalizing $\sigma(\phi)$ of (18a), results in

$$\frac{\sigma}{\sigma_0} = \frac{1-\phi}{1-\phi_0}\sqrt{\frac{\log(1-\phi)}{\log(1-\phi_0)}} \ , \tag{18b}$$

a relation now independent of D_0. (In the DNS results, σ_0 in its normalized surface-to-volume ratio is specified directly by the initial surface-to-volume ratio of the preform geometries, which is the same for all layup configurations considered here.) The values of the Thiele modulus for which Eq. (18) is valid, *i.e.*, accurately predicts the surface-to-volume ratio in an actual growing fiber geometry, is unknown.

Microstructural models have also been developed specifically for woven fiber preform geometries, but assume non-interacting deposition fronts or slow chemistry ($K << 1$). A representative example here is the model of Sheldon & Besmann [8]:

$$\frac{\sigma}{\sigma_0} = \frac{\phi}{\phi_0}\exp\left[-\left(\frac{1-\phi_0}{\phi_0}\right)\left(\frac{D^2}{D_0^2}-1\right)\right] \tag{19a}$$

$$\frac{D}{D_0} = \sqrt{1-\left(\frac{\phi_0}{1-\phi_0}\right)\log\left(\frac{\phi}{\phi_0}\right)} \ , \tag{19b}$$

where subscript "0" refers to the initial value of the property. Since the deposition fronts cannot merge, a single, effective lengthscale D characterizes the densifying preform at all times.

Figure 5 compares models Eq. (18) and Eq. (19) to the DNS data. Symbols show the nondimensional surface-to-volume ratio (σ/σ_0) against the normalized porosity (ϕ/ϕ_0) at regular time intervals from the DNS experiments. Black circles represent the Baseline preform geometry case. Figure 5 shows that a lower ultimate porosity is reached at the lower Thiele modulus, as physically described in the discussion surrounding Figs. 2–4. Magenta lines in Fig. 5 are the analytical functions: The upper (dash-dot) line is Eq. (18) and the lower (dash-dash) line is Eq. (19). Equation (18) predicts that σ/σ_0 exceeds unity, while Eq. (19) shows that σ/σ_0 always decreases with porosity for the preform geometries considered here.

The DNS results from the other two preform geometries are also shown in Fig. 5: Blue squares represent the Overlap case and red triangles represent the Aligned case. Focusing first on the results from the Baseline preform (black circles) of Fig. 5, a clear Thiele modulus depedence is observed. At relatively high Thiele modulus ($K = 0.1$), the surface area initially increases, then decreases just before the ultimate porosity is reached. This trend is captured by model Eq. (18), although some discrepency arguably exists in the exact magnitudes. At low Thiele modulus ($K = 0.001$), the surface area of the Baseline preform monotonically decreases for all CVI densification times. In this limit, both trends and magnitudes are not described well by Eq. (18), while Eq. (19) predicts a qualtatively similar behavior to the DNS simulation results. Quantitatively, Eq. (19) overpredicts the partially-densified surface areas. An increase in the Thiele modulus to an intermediate value $K = 0.01$ seems to alleviate some of the discrepency.

Models given by Eq. (18) and Eq. (19) seem to roughly represent the limiting behavior with respect to Thiele modulus for all densified preform geometries shown in Fig. 5. Perhaps an exception is the Aligned case, where at $K = 0.1$, Eq. (19) does a better job of describing the densified surface area dependence on porosity. No DNS simulations were performed for $K > 0.1$.

The main conclusion from Fig. 5 is that the microstructural properties depend upon finite Thiele modulus effects. This means microstructural models which either implicitly assume slow chemistry, like Eq. (19), or do not explicitly account for finite Thiele modulus effects, like Eq. (18), are not able to generally describe the microstructural properties during CVI densification. The DNS-based correlations of Fig. 5 can be used directly in the mean-field CFD simulations of fiber-woven porous media.

3.2 Flow infiltration properties

The flow infiltration properties, B and $\mathcal{D}_{\text{eff},j}$ in Eq. (2), can be characterized by laboratory experiments. This is accomplished by partially densifying the preform of interest via CVI processing, then employing an inert gas apparatus to flow test the partially-densified specimens. This approach can obviously become costly given the diversity of preform geometries and variety of partially-densified states. The number of experimental trials becomes particularly large if the scaling of the infiltration characteristics is to be accurately quantified.

The present DNS simulations provide a relatively inexpensive method to supplement such experimental investigations at a small fraction of the cost. Since the densified geometry is available at any given time from the level-set field, the partially-densified preform can be treated as any generic solid model for CFD simulations conventionally employed by industry, *i.e.*, using basic laminar flow calculations.

Employing the conventional CFD simulations, the permeability is computed from Darcy's law:

$$\frac{\Delta p}{L} = -\frac{1}{B}\mu u_0 \ , \tag{20}$$

where Δp is the pressure loss across distance L due to the viscous fluid. The fluid has constant absolute viscosity μ and constant density. The massflow rate is fixed with initial velocity u_0 set in the through-thickness direction at the inflow boundary. Figure 6 shows an illustrative pressure field from such a calculation for a fixed preform geometry characterized by D, σ, and ϕ. Varying a fluid property or u_0 in Eq. (20) while keeping the geometry fixed, yields a linear relationship to directly compute the inverse of the permeability, $1/B$. The Reynolds number must be low in the CFD simulations to avoid the inertial losses neglected by Eq. (20).

Similarly, the effective diffusivity is computed by solving, for a fixed geometry, the binary Fickian diffusion problem illustrated in Fig. 7. At steady-state, the averaged concentration gradients in the through-thickness direction (dY_1/dz) of either inert gas becomes approximately constant. Fick's first law, used to model the diffusive gas transport in the CFD, describes the mass flux as

$$J_j = -\mathcal{D}_{12}\frac{dY_j}{dz} \ , \tag{21}$$

where $\mathcal{D}_{12}$ is the constant binary diffusion coefficient. Write Fick's law inside of the porous media as $J_{j,\text{inside}} = \mathcal{D}_{\text{eff}}(dY_j/dz)_{\text{inside}}$ and outside as $J_{j,\text{outside}} = \mathcal{D}_{12}(dY_j/dz)_{\text{outside}}$. From continuity, the mass fluxes can be equated to yield the ratio of the effective diffusivity to bulk diffusivity as

$$\frac{\mathcal{D}_{\text{eff},j}}{\mathcal{D}_{12}} = \frac{(dY_j/dz)_{\text{outside}}}{(dY_j/dz)_{\text{inside}}} \ . \tag{22}$$

The CFD calculations are repeated for different partially-densified preform geometries to develop the scaling relationships.

Figure 8 shows the permeabilities and effective diffusivities of the densified preforms at regular CVI processing time intervals up to the completion time, when the ultimate porosity has been reached. The three preform designs (Baseline, Overlap, and Aligned preform geometry configurations) are the same as those described in the discussion surrounding Fig. 5. In all cases shown in Fig. 8, the Thiele modulus is fixed at $K = 0.001$. For reference, the magenta dash-dash lines show ϕ scaling dependencies: $\sim \phi^3$ and ϕ^4 in Fig. 8 (a), and $\sim \phi^1$ and ϕ^2 in (b).

The commonly accepted scaling of the infiltration properties are

$$\sigma^2 B \sim \phi^3 \quad \text{and} \quad \frac{\mathcal{D}_{\text{eff},j}}{\mathcal{D}_{12}} \sim \phi \ . \tag{23}$$

These relationships represent the well-known Kozeny-Carman scaling and form the basis of Eq. (2).

Focusing first on results from the Baseline preform (black circles in Fig. 8), an approximate scaling of $\sigma^2 B \sim \phi^m$ and $\mathcal{D}_{\text{eff},j}/\mathcal{D}_{12} \sim \phi^n$ are observed with exponents m and n approximately independent of CVI processing time. However, the commonly accepted scaling exponents given by Eq. (23) underpredict the sensitivity to ϕ in both infiltration properties.

For the other preform geometries (Overlap and Aligned preform geometries), the standard scaling Eq. (23) is not valid across the entire range of ϕ. Recall, the Overlap preform design represents a geometry with a higher geometric tortuosity with respect to the Baseline, while the Aligned preform a lower geometric tortuosity. The results of Fig. 8 say that a simple tortuosity correction (via parameters C_1 and C_2 in Eq. (2)) could not be characterized by an additional ϕ dependence alone, as is commonly resorted to in practice.

An important trend to observe in Fig. 8 is the large range in infiltration characteristics of woven fiber preforms. At a fixed porosity, the permeability can vary by multiple orders-of-magnitude, with the Aligned geometry showing the highest permeability. A relatively large variation is observed in the effective diffusivity as well, with again the Aligned ply preform exhibiting the largest effective diffusivity. Further, while both infiltration characteristics appear to have complex scaling properties, the trends between the two are similar. Figure 9 highlights this latter observation, which shows the direct proportionality between B and $\mathcal{D}_{\text{eff},j}$ as

$$\sigma^2 B \sim \left(\frac{\mathcal{D}_{\text{eff},j}}{\mathcal{D}_{12}} \right)^p \ . \tag{24}$$

Here, $p = 2.40$ (computed in the least-squares sense for the Aligned case), $p = 2.16$ (Baseline), and $p = 1.70$ (Overlap). The sensitivity decreases with increasing geometric tortuosity of the preform geometries considered here.

4 Conclusions

Direct numerical simulations have been performed with the goal of improving CFD modeling of CVI-based manufacturing processes. To simulate the CVI densification process, the competition between the finite-rate chemistry and diffusion processes must be described. With DNS, the Thiele modulus is a fundamental non-dimensional parameter of the governing equations. The virtual DNS experiments performed here show a rich complexity in densification characteristics even for preform geometries with the same initial porosity, surface area, and surface-to-volume ratio. For example, the ultimate porosity and surface-to-volume ratio at any given densified state show a strong dependence on the Thiele modulus and preforming layup strategy (Fig. 5). Further, the different preforming layup strategies can result in different flow infiltration scaling dependencies with porosity, while their magnitudes can differ by an order-of-magnitude (or more) at the same porosity (Fig. 8). The DNS-derived correlations of Figs. 5 and 8 can be used directly in modeled CFD simulations.

The present work represents the first time DNS has been applied to develop CFD porous media models for practical CVI application, *i.e.*, using fit-for-purpose, woven preformed geometries. The DNS allows the densification characteristics to be quantified, also for the first time, throughout the entire CVI densification cycle. However, the present DNS is not without limitations. Convection effects have not been considered in the virtual CVI processing experiments. The seminal CVI work by Besmann *et al.* [30] have shown that forced-flow CVI can reduce the CVI manufacturing time from days to minutes. In the present DNS, only a one-step chemical kinetic model was assumed. Extensive research [15, 16, 17, 18, 19, 20, 21] has established the importance of accounting for both homogeneous and heterogeneous reaction timescales. The continuum first-principles DNS formulation here can readily be extended to include both convective effects and multi-step kinetics, developments which will be made in future work.

Acknowledgements

This research was supported by the High-Performance Computing for Manufacturing Project Program (HPC4Mfg), managed by the U.S. Department of Energy Advanced Manufacturing Office (AMO) within the Energy Efficiency and Renewable Energy Office (EERE). The work was performed using resources of the Oak Ridge Leadership Computing Facility (OLCF) and Oak Ridge National Laboratory, which are supported by the Office of Science of the U.S. Department of Energy under Contract No. DE-AC0500OR22725.

References

[1] R. Sankaran, V. Ramanuj, C. M. Cha, and D. Liliedahl. Level-set modeling simulations of chemical vapor infiltration for ceramic matrix composites manufacturing. Technical report, Oak Ridge National Laboratory ORNL/TM-2019/1206, 2019.

[2] S. Jin and X. Wang. Robust numerical simulation of porosity evolution in chemical vapor infiltration: II. Two-dimensional anisotropic fronts. *J. Comp. Phys.*, 179(2):557–577, 2002.

[3] K. Guan, L. Cheng, Q. Zeng, L. Zhang, J. Deng, K. Li, and H. Li. Modeling of pore structure evolution between bundles of plain woven fabrics during chemical vapor infiltration process: The influence of preform geometry. *J. Am. Ceram. Soc.*, 96(1):51–61, 2013.

[4] N. Reuge and G. L. Vignoles. Modeling of isobaric-isothermal chemical vapor infiltration: Effects of reactor control parameters on a densification. *J. Matls. Processing Tech.*, 166:15–29, 2005.

[5] X. Wei, L. Cheng, L. Zhang, Y. Xu, and Q. Zeng. Numerical simulation for fabrication of C/SiC composites in isothermal CVI reactor. *Comp. Matls. Sci.*, 38:245–255, 2006.

[6] Narottam P Bansal and Jacques Lamon. *Ceramic matrix composites: materials, modeling and technology.* John Wiley & Sons, 2014.

[7] J. Y. Ofori and S. V. Sotirchos. Structural model effects on the predictions of chemical vapor infiltration models. *J. Electrochem. Soc.*, 143(6):1962–1973, 1996.

[8] B. W. Sheldon and T. M. Besmann. Reaction and diffusion kinetics during the initial stages of isothermal chemical vapor infiltration. *J. Am. Ceram. Soc.*, 74(12):3046–53, 1991.

[9] G.-Y. Chung, B. J. McCoy, J. M. Smith, and D. E. Cagliostro. Chemical vapor infiltration: Dispersed and graded depositions for ceramic composites. *AIChE J.*, 39(11):1834–1846, 1993.

[10] T.L. Starr. Gas transport model for chemical vapor infiltration. *J. Mater. Res.*, 10(9):2360–2366, 1995.

[11] K. Guan, L. Cheng, Q. Zeng, Z.-Q. Feng, L. Zhang, H. Li, and H. Ren. Modeling of pore structure evolution within fiber bundle during chemical vapor infiltration process. *Chem. Engr. Sci.*, 66:5852–61, 2011.

[12] S. Torquato. *Random Heterogeneous Materials.* Springer, 2001.

[13] Olivia Coindreau, G Vignoles, and Peter Cloetens. Direct 3d microscale imaging of carbon–carbon composites with computed holotomography. *Nuclear Instruments and Methods in Physics Research Section B: Beam Interactions with Materials and Atoms*, 200:308–314, 2003.

[14] Gerard L Vignoles, Olivia Coindreau, Azita Ahmadi, and Dominique Bernard. Assessment of structural and transport properties in fibrous c/c composite preforms as digitized by x-ray cmt. part ii: Heat and gas transport. *J. Mater. Res.*, 22(6):1537–1550, 2007.

[15] Y. Ge, M. S. Gordon, F. Battaglia, and R. O. Fox. Theoretical study of the pyrolysis of methyltricholorosilane in the gas phase. 1. Thermodynamcs. *J. Phys. Chem.*, 111:1462–1474, 2007.

[16] Y. Ge, M. S. Gordon, F. Battaglia, and R. O. Fox. Theoretical study of the pyrolysis of methyltricholorosilane in the gas phase. 2. Reaction paths and transition states. *J. Phys. Chem.*, 111:1475–1486, 2007.

[17] Y. Ge, M. S. Gordon, F. Battaglia, and R. O. Fox. Theoretical study of the pyrolysis of methyltricholorosilane in the gas phase. 3. Reaction rate constant calculations. *J. Phys. Chem.*, 114:2384–2392, 2010.

[18] G. D. Papasouliotis and S. V. Sotirchos. On the homogeneous chemistry of the thermal decomposition of methyltrichlorosilane thermodynamic analysis and kinetic modeling. *J. Electrochem. Soc.*, 141(6):1599–1611, 1994.

[19] F. Loumagne, F. Langlais, and R. Naslain. Experimental kinetic study of the chemical vapour deposition of SiC-based ceramics from CH_3SiCl_3/H_2 gas precursor. *J. Cryst. Growth*, 155:198–204, 1995.

[20] F. Loumagne, F. Langlais, and R. Naslain. Reactional mechanisms of the chemical vapour deposition of SiC-based ceramics from CH_3SiCl_3/H_2 gas precursor. *J. Cryst. Growth*, 155:205–213, 1995.

[21] K. Dang and H. Chelliah. Thermal decomposition of methyltricholorosilane (MTS)/hydrogen/inert mixtures at conditions relevant for chemical vapor infiltration of SiC ceramics. *J. Chem. Kin.*, Submitted.

[22] S. Jin, X. Wang, T. L. Starr, and X. Chen. Robust numerical simulation of porosity evolution in chemical vapor infiltration I: Two space dimension. *J. Comp. Phys.*, 162(2):467–482, 2000.

[23] S. Jin, X. Wang, and T. L. Starr. A model for front evolution with a nonlocal growth rate. *J. Mater. Res.*, 14(10):3829–3832, 1999.

[24] K. Guan, L. Cheng, Q. Zeng, H. Li, Shanhua Liu, J. Li, and L. Zhang. Prediction of permeability for chemical vapor infiltration. *J. Am. Ceram. Soc.*, 96(8):2445–2453, 2013.

[25] S. Osher and R. Fedkiw. *Level set methods and dynamic implicit surfaces.* Springer, 2002.

[26] J. A. Sethian. *Level set methods and fast marching methods: Evolving interfaces in computational geometry, fluid mechanics, computer vision, and materials science.* Cambridge, 1999.

[27] Vimal Ramanuj and Ramanan Sankaran. High order anchoring and reinitialization of level set function for simulating interface motion. *Journal of Scientific Computing*, 81(3):1963–1986, 2019.

[28] Vimal Ramanuj, Ramanan Sankaran, and Balasubramaniam Radhakrishnan. A sharp interface model for deterministic simulation of dendrite growth. *Computational Materials Science*, 169:109097, 2019.

[29] H. Carter Edwards, Christian R. Trott, and Daniel Sunderland. Kokkos: Enabling manycore performance portability through polymorphic memory access patterns. *Journal of Parallel and Distributed Computing*, 74(12):3202 – 3216, 2014. Domain-Specific Languages and High-Level Frameworks for High-Performance Computing.

[30] TM Besmann, BW Sheldon, RA Lowden, and DP Stinton. Vapor-phase fabrication and properties of continuous-filament ceramic composites. *Science*, 253(5024):1104–1109, 1991.

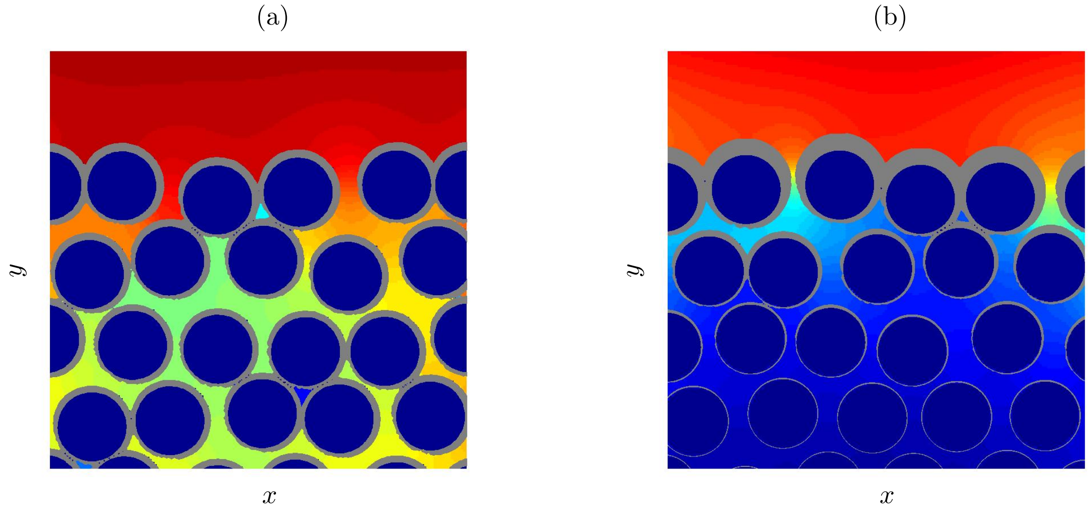

Figure 1: Two limiting (unoptimized) chemical vapor infiltration processes. In (a), the chemical timescale is much larger than the transport of vapor. In this case, there is good uniformity in the growth of the matrix material (grey), but at the costly expense of a long manufacturing time. In (b), the chemical timescale is relatively much smaller, which does not allow matrix growth to occur inside the preform due to blockage of vapor infiltration. Red contour colors are highest vapor concentrations. At the same total matrix weight gain as in (a), large "inaccessible" pores make parts from process (b) poor quality and therefore costly.

(a) Preformed geometry

(b) Densified weave at $K = 0.001$

(c) Densified weave at $K = 0.1$

Figure 2: Initial (a) and partially-densified woven preforms from the DNS simulations. Figures (b) and (c) show the densified weave after processing. In (b), the Thiele modulus is $K = 0.001$ and the chemical time scale is much larger than transport of vapor. In (c), $K = 0.01$ and the chemical timescale is relatively much smaller.

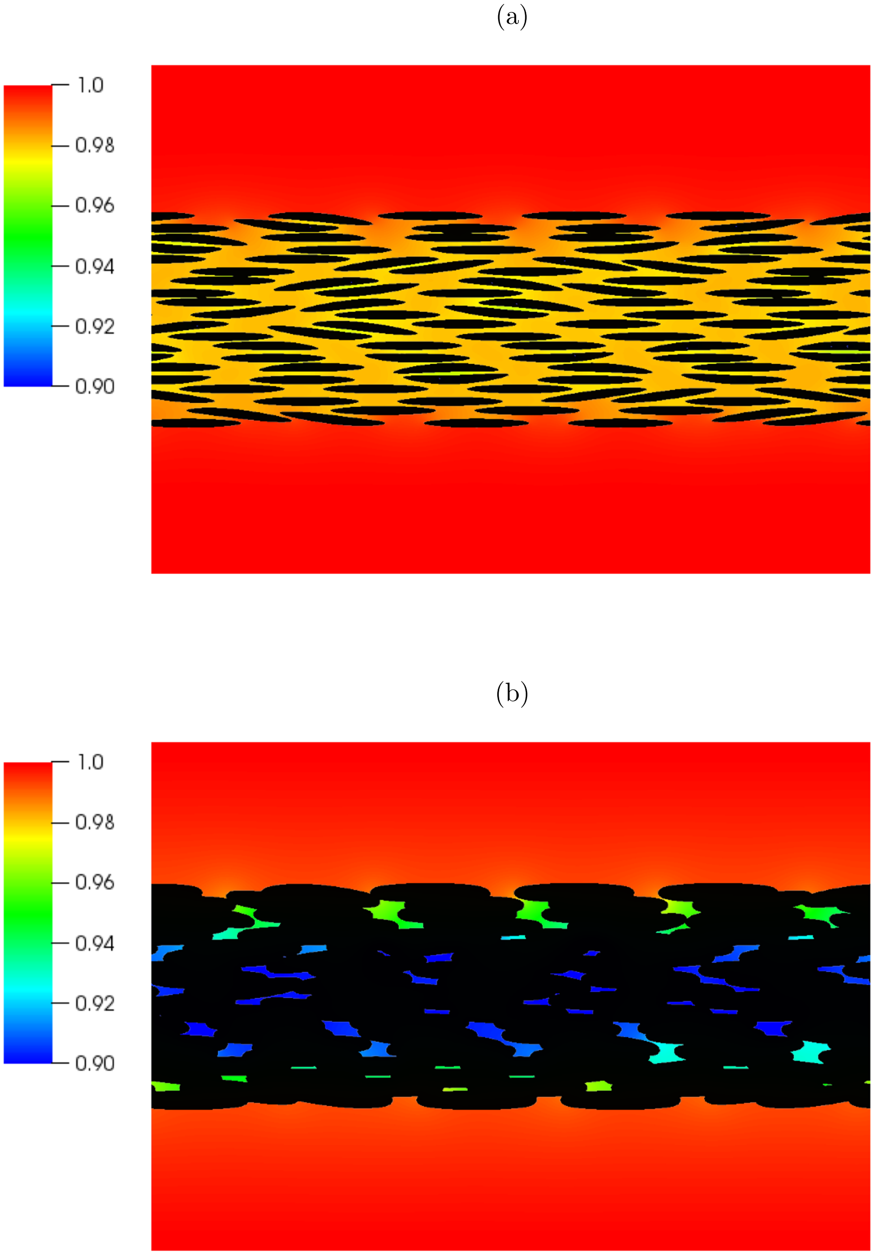

Figure 3: Cross-section of (a) the initial and (b) processed weave for the $K = 0.001$ case shown in Fig. 2. Black region represents the solid phase. Also shown is the scalar transported through the porous matrix as pseudocolor in the rainbow color scale.

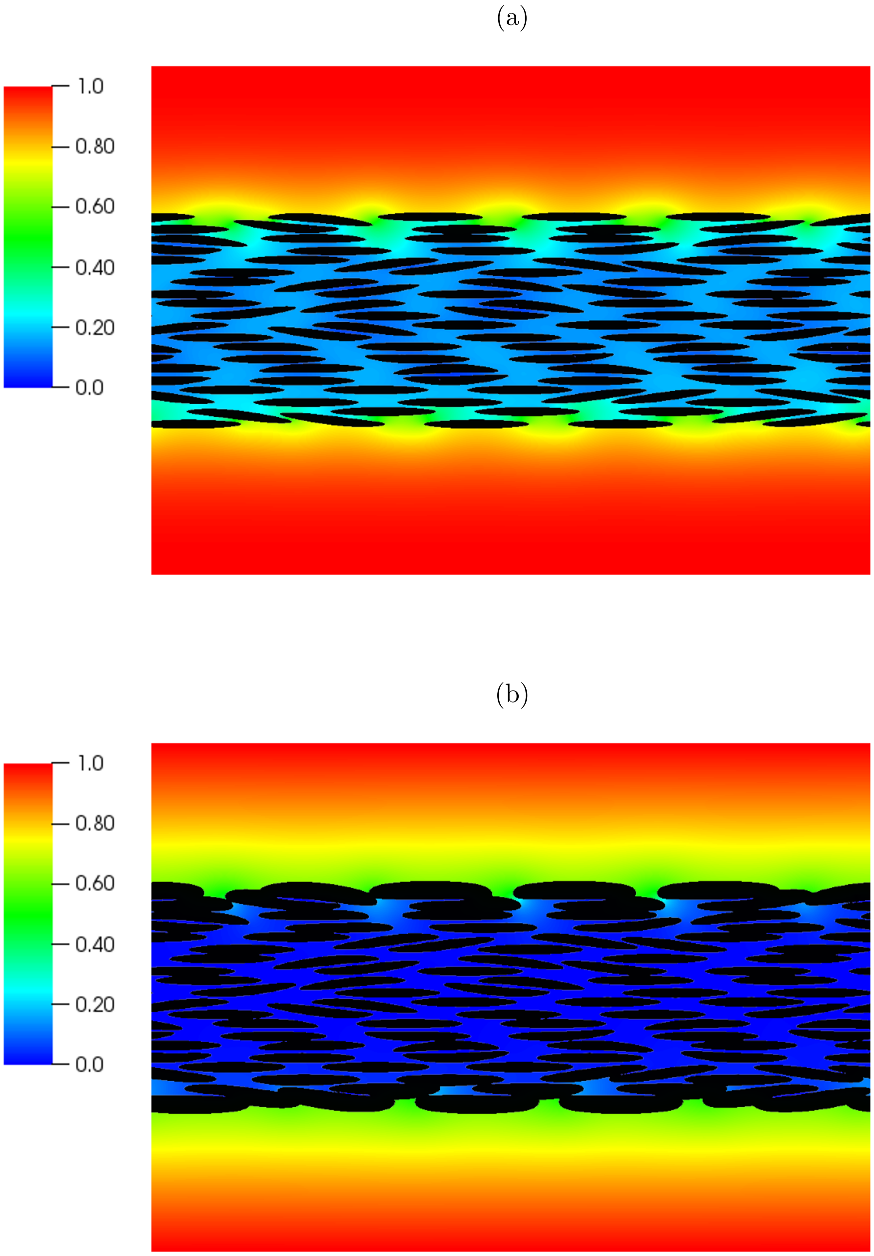

Figure 4: Cross-section of (a) the initial and (b) processed weave for the $K = 0.1$ case shown in Fig. 2. Black region represents the solid phase. Also shown is the scalar transported through the porous matrix as pseudocolor in the rainbow color scale.

(a) $K = 0.1$

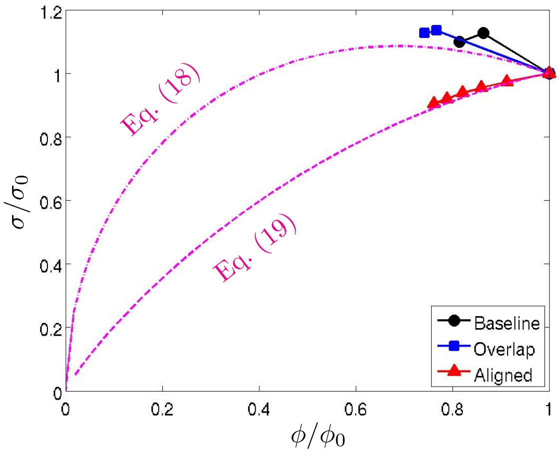

(b) $K = 0.01$

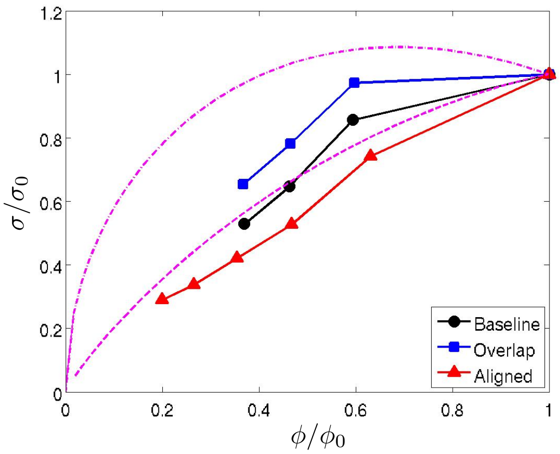

(c) $K = 0.001$

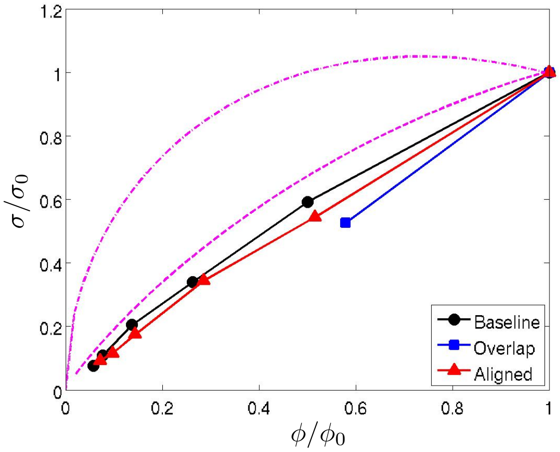

Figure 5: Deposited surface area dependence on porosity for decreasing Thiele moduli: (a) $K = 0.1$, (b) $K = 0.01$, and (c) $K = 0.001$.

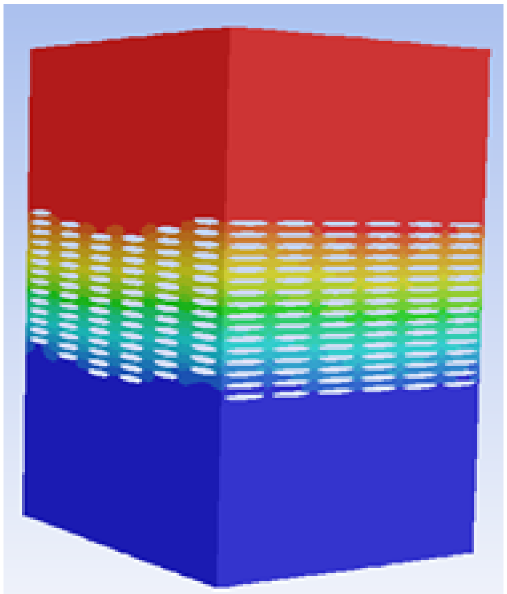

Figure 6: Steady-state pressure field (high: red and low: blue) used to compute weave permeability.

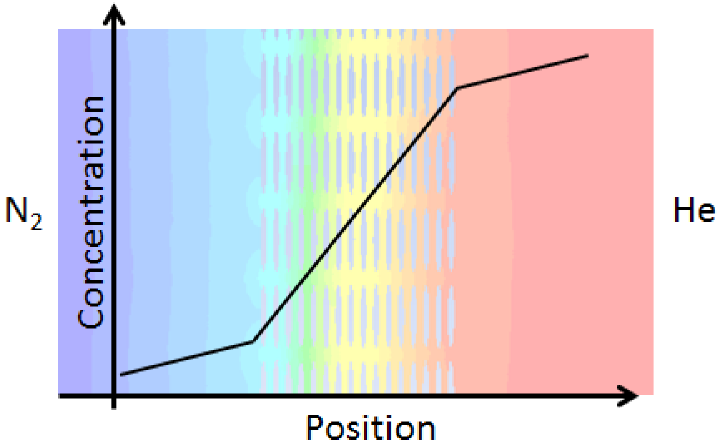

Figure 7: Inert species concentrations used to compute effective diffusivity through the weave. The domain is subject to N_2 diffusion from the left and He from the right. Color scale (high: red and low: blue) and the black line show the steady-state He concentraion.

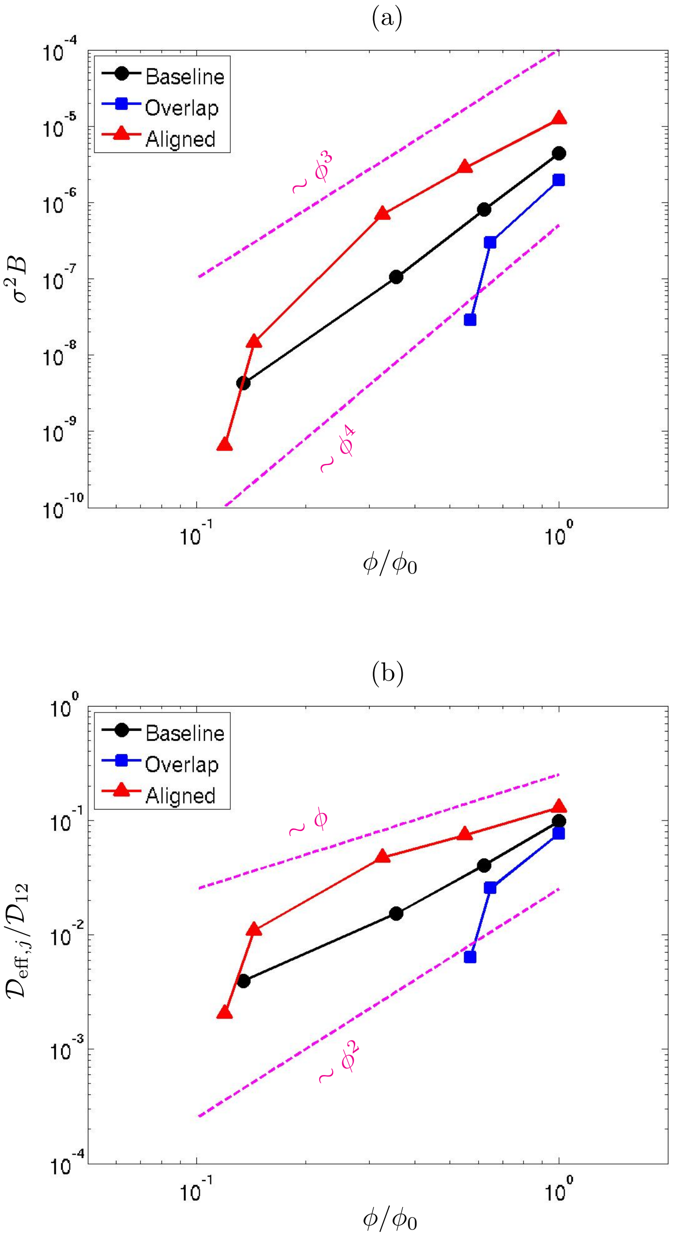

Figure 8: Permeability (a) and effective diffusivity (b) scaling with porosity for the three different preform geometries.

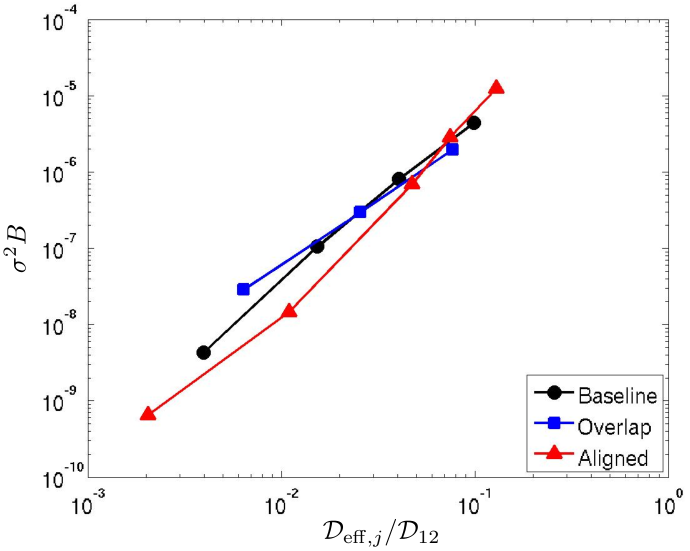

Figure 9: Proportionality of permeability to effective diffusivity.